Regional Studies in Marine Science 45 (2021) 101798

Contents lists available at ScienceDirect

Regional Studies in Marine Science

journal homepage: www.elsevier.com/locate/rsma

Seasonal to decadal scale shoreline changes along the Cameroonian coastline, Bay of Bonny (1986 to 2020)

Njutapvoui F. Nourdi [a,c,*], Onguene Raphael [d], Abessolo O. Grégoire [c], Rudant Jean Paul [b], Bogning Sakaros [d], Stieglitz Thomas [e,f], Tomedi E. Minette [c]

[a] IRGM Institute of Geological and Mining Research, Vogt Street, BP: 4110 Yaoundé, Cameroon
[b] Université Gustave Eiffel, IGN, LaSTIG/Acte, 5 Bd Descartes, Champs sur Marne, 77455 Marne la ValléeCedex 2, France
[c] Ecosystems and Fishery Resources Laboratory, Institute of Fisheries and Aquatic Sciences, University of Douala, BP 2701 Douala, Cameroon
[d] Laboratory of Technology and Applied Science, University Institute of Technology, University of Douala, BP 8698 Douala, Cameroon
[e] Aix-Marseille Université, CNRS, IRD, INRAE, Coll France, CEREGE, Aix-en-Provence, France
[f] Centre for Tropical Water and Aquatic Ecosystem Research TropWATER, James Cook University, Townsville, QLD, Australia

ARTICLE INFO

Article history:
Received 10 September 2020
Received in revised form 17 April 2021
Accepted 17 April 2021
Available online 26 April 2021

Keywords:
Coastline
Wave climate
Bay of Bonny
Optic
Ecosystems

ABSTRACT

The Bay of Bonny, located along the Cameroon coastline, is home to diverse ecosystems. It is under significant pressure from large human activity, but remains very little studied, like much of the Gulf of Guinea. In order to understand its long-term shoreline variations and the role the wave regime plays in the evolution of the coastline, a study was conducted on the basis of optical image archives from Landsat 5/7/8 and Sentinel-2A/2B satellite missions acquired between October 1986 and May 2020, coupled with daily ERA-Interim wave re-analysis data covering the period from January 1986 to August 2019. Overall, the results show that the evolution of the coast is highly variable in space and time, as indicated by different levels of erosion (30.55 %), and accretion (27.7 %) on the decadal-scale, with the most significant variations occurring in estuarine areas. Nevertheless, 41.75% of the Cameroon shoreline remains stable during the study period. Three main periods (1986–1994; 1995–2005; 2006–2020) during which the coast underwent significant changes a different location were identified, reaching a retreat rate of up to −10 m/year in the northern section during the first period 1986–1994. The annual trend of significant wave heights anomaly along the coast (−5.6 to −4.1 mm/year) with wave height maxima estimated at 1.46 ± 0.65 m, where observed during the summer months (July–August). Monthly shoreline changes are inversely correlated with wave climate in some segments. Eigenvalue orthogonal decomposition analyses (Mode 1, Empirical Orthogonal Function) show that 76.3% of the observed variability would be due to the relatively strong local influence of erosion and accretion. This local influence can be related to wave regime at shorter timescale (monthly to seasonal) and the sediment variability from the source inland to the coast at longer timescale (seasonal to decadal). These observations explain a complex pattern of shoreline changes with an almost continuous retreat shoreline during the period 1986–2013 and a reversal in trend towards accretion during the period 2013–2020. EOF mode 2 explains 23.7% of variability, which can be potentially associated with the synergetic relationship between tidal currents and wave-induced longshore current, tidal currents and possibly pockets of human activity. This is attributed to an overall decrease in the supply of sediment via the coastal transport system that prevails in the Gulf of Guinea.

1. Introduction

Coastal areas around the world are increasingly anthropized and inhabited because of their socio-economic and recreational importance (Boateng, 2009, 2012). Several recent studies (Luijendijk et al., 2018; Kuenzer et al., 2014; Dada et al., 2015, 2016) have shown that these environments are also subject to varying degrees of natural and anthropogenic morphological variation, thereby increasing the vulnerability of these areas and the risks to property and people (Richards and Nicholls, 2009). The very high vulnerability of some coastal environments remains a major concern (Bosom and Jiménez, 2011; Tano et al., 2016) in view of the intensification of extreme wave and surge events and sea level rise due to climate change (Pilkey and Cooper, 2014; Ranasinghe, 2016; Anthony, 2017). Tropical coastal environments are particularly affected by erosion and flooding, but their variability

* Corresponding author at: IRGM Institute of Geological and Mining Research, Vogt Street, BP: 4110 Yaoundé, Cameroon.
E-mail addresses: njutapvouinourdi@yahoo.fr (N.F. Nourdi), ziongra@yahoo.fr (O. Raphael), gregsolo55@yahoo.fr, gregoireabess@gmail.com (A.O. Grégoire), jean-paul.rudant@u-pem.fr (R. Jean Paul), sakarosb@gmail.com (B. Sakaros).

https://doi.org/10.1016/j.rsma.2021.101798
2352-4855/

and vulnerability are still poorly understood, especially on long time scales (decades), due to the lack of adequate morphological and hydrodynamic data. Coastal management policies in these regions are, more often than not, limited to local scale and not well informed to support sustainable coastal development on a large spatial scale, as shown by Ndour et al. (2018).

In West Africa, studies have been carried out on coastal zone dynamics to assess its vulnerability. Almar et al. (2014) demonstrated the importance of understanding the causes of erosion observed in the Bay of Benin on several scales, Anthony and Blivi (1999), Laibi et al. (2014) and Anthony et al. (2019) demonstrated the impact of the presence of ports and coastal infrastructures. The work of Dada et al. (2016) has led to an understanding of the wave climate, its potential changes and its implications on coastal evolution for environmental monitoring and sustainable management of the Niger Delta. In addition, several major projects have been launched in West Africa, including the West African Coastal Observation Mission (MOLOA, 2013), aimed at an integrated coastline management strategy, including the production of historical data on coastal dynamics and risks in coastal areas. Giardino et al. (2018) and Ndour et al. (2018) proposed a large-scale coastal policy for the development of sustainable management practices in coastal areas, but this is difficult to implement, because there is not real integrated national management strategy for coastal zones in West and Central Africa which leads to a rapid expansion linked to demographic pressures, the construction of a seaports, hydroelectric dams, anarchic construction which affect the stability of the coast.

Along the Cameroon coastline, few studies have been carried out on coastal dynamics. Abessolo Ondoa et al. (2018) have studied coastal erosion/accretion processes through the modelling of barotropic currents in the Wouri estuaries in central Cameroon. The recent work of Fotsi et al. (2019) on the temporal (1948–2012) and dynamic evolution of the Wouri estuary's coastline have demonstrated the influence of the sedimentary regime. These studies have shown that the Cameroonian coastline has undergone complex patterns of shoreline modification. However, regional-scale sustainable coastal zone management is hampered by a general lack of continuous and accurate historical data on the position of the coastline. It is difficult to study the impact of hydrodynamic forcing on the Cameroonian coastline due to the lack of morphological data. More importantly, the multi-scale nature of wave impact: event-driven (impact of storms and waves, and tides); seasonal (seasonal behaviour of the coastline); interannual to decadal trend (difficult to observe due to lack of adequate data) remains almost unknown on this coast.

Given the current lack of data and understanding of coastline dynamics in the Bay of Bonny, the objective is to study shoreline variations over the last 34 years (1986 to 2020) and the role of wave climate in coastal changes. In addition, other important factors that could affect coastal dynamics will be explored.

2. Materials and methods

2.1. Study site

The study area is located between Rio-del-Rey (Cameroon) to Campo (Equatorial Guinea) and covers entire Cameroonian coastline in the Bay of Biafra (Fig. 1). This coast is characterized by different ecosystems. Ten major rivers flow into the ocean, the most important of which are Ntem, Nyong, Sanaga Wouri and the Rio del Rey. The Table 1 below summarizes the characteristics of the most important rivers on the Cameroonian coast (Olivry, 1986; Onguene, 2015).

Following Giresse et al. (1996) four subsets (S-E) of the coast were defined (Fig. 1), as follows:

Table 1
Characteristics of some coastal rivers of Cameroon.

River	Annual flow ($\times 10^{10} m^3$/year)	Watershed (km^2)
Rio del Rey	2.8	17,194
Sanaga	6.2	131,500
Wouri	1.7	8,250
Nyong	1.4	26,400
Ntem	1.6	26,350

— Subset 1: Composed of the Rio del Rey and Cross river basins bordering the east of the Bakassi peninsula in Cameroon, this complex is considered as an extension of the eastern zone of the Niger delta set up during the Paleocene-Eocene. It contains the largest zone of mangroves (125,259 hectares) in the country (Ajonina, 2010; MINEPDED-RCM, 2017) and a group of islets. The Rio del Rey's estuary is open and shallow, with tidal ranges reaching up to 3 m during the rainy season (March to October).
— Sub-group 2 (Idenau to Limbé): This section is characterized by small basalt cliffs (4–8 m) separated by small bays with pebble (10–20 cm) and sand beaches on the volcanic base of Mount Cameroon. Otherwise, narrow coastal barrier bar the outlets of small rivers in veritable lagoons of mouths invaded by mangroves (Morin and et Kuété, 1988).
– Subset 3 (Cameroon estuary): with an area of 103,817 ha (ONEQUIP, 2009), it constitutes a vast wetland, 30 km long and almost as wide; it is an integral part of the Wouri watershed. The relief is formed by a succession of sedimentary plains. This bay is also bordered by the second largest mangrove area (93,549 hectares) (MINEPDED-RCM, 2017), and is the receptacle of the main rivers of the region (Wouri, Mungo and Dibamba). Areas of the bay characterized by high flow velocities show a maximum range of 3 m (Onguene et al., 2015).
— Subset 4 (Kribi-Campo): From the mouth of the Nyong to the Ntem River, this coast is characterized by the presence of sandy beaches, which alternate with rocky headlands, lagoons, mangroves and other coastal vegetation. It contains two protected areas (Douala-Edea Wildlife Reserve and Campo-Ma'an National Park). The tidal range is about 1.8 m at Campo, 1.5 m at Kribi and 1.2 m at Petit-Batanga (Giresse et al., 1996).

2.2. Landsat and sentinel-2 image extraction and processing under DSAS

We extracted a set of 10 images with less than 10% cloud cover (a common problem in the tropics), i.e. 7 images from Landsat 5/7/8 missions downloaded from https://earthexplorer.usgs.gov/ and 3 images from the Sentinel 2A/2B satellites downloaded from the Copernicus platform of the ESA (European Space Agency). All Landsat satellites are orbiting at an altitude of 705 km with a swath of 185 km/185 km (Fernand et al., 2002). The "Sentinel-2" constellation, on the other hand, consists of two satellites (Sentinel-2 A and Sentinel-2B), at an altitude of 786 km and a swath of 250/250 km. Orbiting on the same sun-synchronous trajectory, but with a phase shift of 180° with respect to each other. The revisit time is 10 days for each satellite (Table 1), which corresponds to 5 days for the couple S-2 A and S2-B. A summary of the different characteristics of the images is given in Table 2.

A series of digital pre-processing was carried out on all the images, ranging from geo-referencing, resetting the images of the various sensors, atmospheric and radiometric correction, contrast enhancement, and the application of a cloud mask to eliminate all images that exceed a certain percentage of cloud cover (include a reference that describes this approach). The quality of the satellite images was improved to obtain optimal detection of the coastline by pan-sharpening (combining the visible band (30 m for Landsat

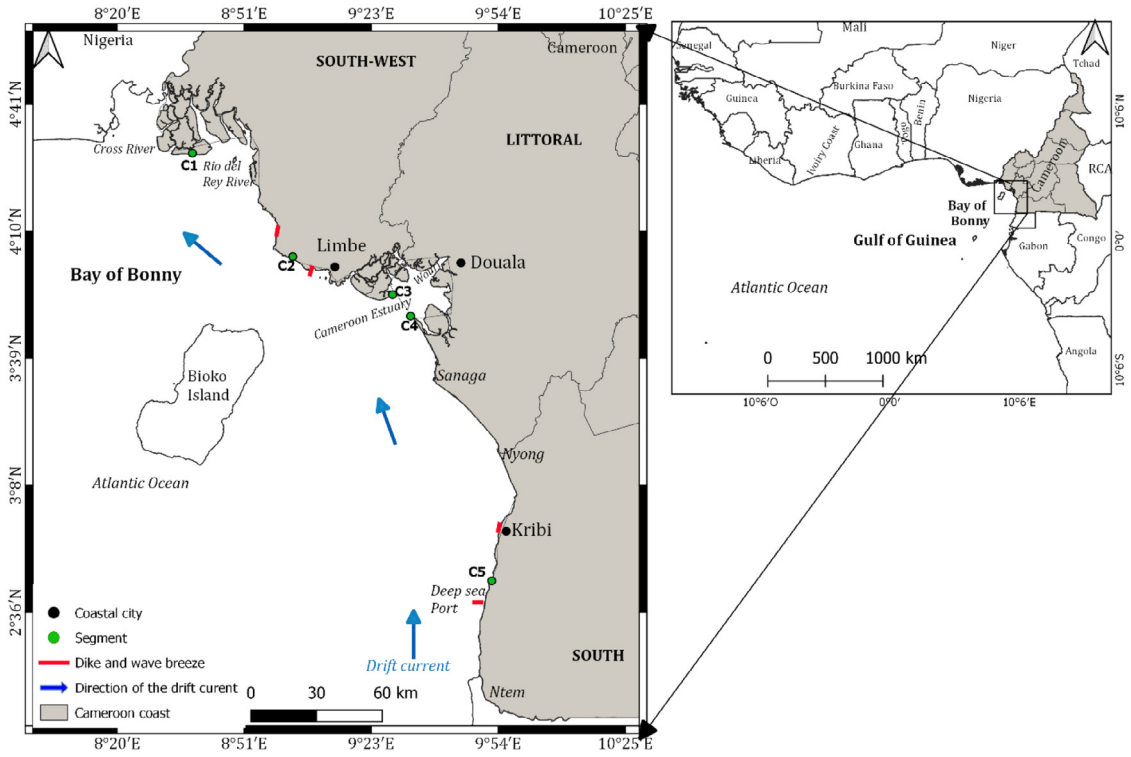

Fig. 1. The coast of Cameroon in Bay of Bonny. The study area extends from the mouth of the *Ntem* (border with Equatorial Guinea to the south) to the Rio del Rey at the Nigerian border. This mesotidal coast is dominated by waves and regional current that generate a strong N–NW longshore drift. The three main cities of the coast, Kribi, Douala and Limbe, are shown in black dot and the segment are shown in green dot, the protective structures (dyke, wave breaker) are represented in small red bar. (For interpretation of the references to colour in this figure legend, the reader is referred to the web version of this article.)

Table 2
Summary of the satellite images used in this study.

Satellite mission	Sensors	Revisit period	Pixel size and band used	Acquisition Date (yyyy/mm/dd)	Cloud cover (%)	Number of images
Landsat 5	TM		30 m, Bands: R (B3), G (B2),	1986/01/26	3.6	2
			B (B1) NIR (B4), SWIR1 (B5, B7)	1996/03/23	4.2	
Landsat 7	ETM+		30 m, Bands: R (B3), G (B2), B (B1) NIR (B4),	1999/12/17	2.4	3
		16 days	SWIR1 (B5, B7) +15 m panchromatic band	2005/03/27	6.2	
				2010/02/14	1.24	
Landsat 8	OLI		30 m, Bands: R (B3), G (B2), B (B1) NIR (B4),	2013/12/22	5.14	3
			SWIR1 (B5, B7) +15 m panchromatic band	2016/03/27	1.33	
				2018/02/03	6.31	
Sentinel 2A/2B	MSI	5 days (Couple	10 m Bands: R(B4), G(B3), B(B2)	2015/11/29	5	3
		S-2A and S-2B)	NIR (B8) +20 m SWIR1 (B12, B11)	2017/05/07	2.42	
				2020/05/26	0.97	

TM (Thematic Mapper), ETM+ (Enhanced Thematic Mapper), OLI (Operational Land Imager), MSI (Multi-spectral instrument); R: red, G: green, B: blue, NIR: near infrared, SWIR: short wave infrared. B1–B12: spectral bands.

and 10 m for Sentinel 2) with the panchromatic band (15 m for Landsat and 10 m for Sentinel). After this step, all bands were reduced to 15 and 10 m for the pixel size of Landsat 7&8 and Sentinel 2A/B respectively, in order to obtain images with better image quality while decreasing as much as possible the digital precision error.

Subsequently, image mosaics were created in order to obtain overall images of the study area. A coloured composition of the bands of each sensor was performed (Table 1 column 3), in order to choose the most appropriate channel to extract the indicator used as a coastline marker (Robin, 2002). Classically, shoreline detection is carried out either in the near infrared or mid-infrared due to the low reflectance of water in the infrared range of the electromagnetic spectrum. On this basis, in order to best highlight the contact between the dry sediments of the high beach and the vegetation cover a coloured composition of the spectral bands was therefore used to discriminate the high beach/vegetation interface (Robin, 2002).

To calculate and map the overall coastline displacement rate, the Digital Shoreline Analysis System (DSAS) plug-in version 4.3 (Thieler et al., 2009), in ArcMap software, shoreline detection and extraction was performed manually by scanning the visible vegetation line and using 1986 as the baseline, the rates of shoreline change for 1999, 2005, 2010, 2013, 2015, 2016, 2017, 2018, and 2020 were calculated. All extracted coastlines were projected to the World Geodetic System UTM 32N reference system (WGS 84). After selecting the 1986 reference line (baseline), the transects were projected from this line at 500 m intervals which intercepted each coastline initially vectorized. The Net Shoreline Movement (NSM), the End Point Rate (EPR) and the Linear Regression Rate (LRR) statistics incorporated in DSAS were calculated to estimate the shoreline variation for the entire study period. We also specified for each coastline a global uncertainty value (+/−5 m) which accounts for the positional and measurement uncertainties.

2.3. Landsat and sentinel-2 image extraction and processing with the CoastSat Toolbox

In order to obtain a longer and less constraining time series, to study the temporal across-shore variability of the coastline in each segment (C1 to C5 Fig. 1), we used a stack of 425 images between the period January 1986 to May 2020 with an average of one image per month retrieved from the Google Earth Engine (GEE) platform via the open-source CoastSat toolkit (Python version 3.6). This Toolbox allowed us to obtain time series data each year of the shoreline position with a horizontal accuracy of 10 m any sandy coastline worldwide (Vos et al., 2019a,b) (see Table 3).

This algorithm allows to retrieve TOA (Top-of-Atmosphere) reflectance images from the GEE archives of Landsat 5/7/8 and Sentinel-2 satellites; and subsequently perform pre-processing of multi-spectral images (cloud masking, pan-sharpening, classification) as described in (Vos et al., 2019a,b). Unlike DSAS, the Coastsat toolbox performs an automatic extraction from a single reference line (baseline) digitized by the user. It then generates the line for each of the sub-pixel resolution images (Van der Walt et al., 2014). However, the results only become useable after applying a tidal correction (Eq. (2)), which is not implemented in the toolbox as it is specific to each area (Vos et al., 2019a,b). The user has the option of choosing a profile in which the time series of the cross-shore distance along the user-defined normal coastal transects is generated.

2.4. Estimation of errors associated with the position of the coastline

To constrain coastline change rates, we estimated four sources of error based on the method of Hapke et al. (2010), i.e. uncertainties associated with georeferencing, digitization, satellite position and tidal water level uncertainty. The mean values for each uncertainty term are presented in Table 2.

The error in digitizing the coastline depends on several factors including the quality of the reference data; the accuracy of the digitization (operator application); the expertise of the operator in interpreting the reference data.

Following Moore and Griggs (2002), the total error related to digitizing (Eq. (1)) can be estimated by the sum of the mean ($\overline{X}$) of the offsets recorded during the repetition of the digitization and 2 standard deviations (2σ) :

$$E_d = \overline{X} + 2\sigma \tag{1}$$

To obtain the errors induce by differences in tidal range associated with the various satellite images, it is recommended that along coasts with large tidal ranges and/or flatter beach profiles, all shorelines be adjusted to a standard reference elevation (Stafford and Langfelder, 1971). Since all images are acquired between 09:00 and 10:00 local time, but at different stages of the tide, a linear tidal correction can be applied using the measured water levels and the characteristic beach slope to translate each shoreline into a reference elevation as follows:

$$E_t = \frac{Z_{ref} - Z_{wl}}{tan\beta} \tag{2}$$

E_t is the horizontal offset across the normal transect to the coast, Z_{ref} is the reference elevation (e.g. 0 m above mean sea level) and Z_{wi} is the local water level at the time of image acquisition, and $tan\beta$ is the beach slope. The precise time of image acquisition to obtain the local water level is stored in the image metadata.

Field work carried out on the beaches of the southern part of Cameroon (Kribi) showed that the typical average slope $tan\beta$ is 0.057 or (5.7%). The significant wave height (Hs) provided by ERA-Interim shows an overall average of 1.04 m off the coast. Tide levels remain relatively low ($\leq$2 m). Thus, for example, the Landsat 8 image of 06 June 2013 was recorded at 09 h 41 min coinciding with a tidal level of 0.4 m. The error (Eq. (3)) is considered here as the sum of the squares of the different sources of error mentioned above (See Table 4):

$$E_i = E_g^2 + E_t^2 + E_d^2 + E_p^2 \tag{3}$$

E_i error of time period i $\{1, 2, \ldots, n\}$

$$ET = \sqrt{(E_{i1}^2 + E_{i2}^2 + E_{i3}^2)}; \tag{4}$$

E_T error for each period

$$EA = \frac{\sum ET}{T2 - T1}; \tag{5}$$

EA: annual error; T time difference.

2.5. In-situ data and processing

Given the near absence of field data on the coast, daily topographic survey campaigns using theodolite and GPS were carried out from 9 to 30 April in the Kribi area (C5), and from 13 to 31 May for the Limbé area (C2). Data was recorded at low tide in order to set the reference height Z = 0 with respect to the mean sea level. We performed a resetting and georeferencing in a Mercator WGS84 projection system with an absolute planimetric accuracy of less than 5 m. This was done in order to bring all the data into the same geographic coordinate system as the satellite data. An instantaneous long-shore and cross-shore average over a 100 m interval was necessary to reduce the error of the coastline position during the survey.

2.6. Extraction and processing of era-interim wave data

Wave parameters (significant height Hs, period Tp and direction) were extracted from the server of the European Centre for Medium-Range Weather Forecasts (ECMWF/ECMWF https://apps.ecmwf.int/datasets/data/interim-full-daily/) on a 0.125° × 0.125° grid, with a time delay of one day resolution, from January 1986 to August 2019. These data are part of the ERA-Interim dataset from the Ers-1&2, Envisat, Jason-1&2 altimetry missions, which involves the analyses of global meteorological variables (Dee et al., 2011; Sterl and Caires, 2005). These data have been widely validated against buoys and altimetry data (Sterl and Caires, 2005), with maximum wave height (Hs > 5 m) and minimum wave height (Hs < 1 m) tending to be under and overestimated respectively (Caires et al., 2006). Fortunately, extreme wave conditions are generally not observed in the relatively constant wave regime in the Gulf of Guinea.

We extracted the time series of Hs for the grid points closest to the coast and then used time averages of the wave parameters for each segment (C1 to C5) over a period of 33 years. However, as largest do not reach the Cameroonian coast, we used the formula proposed by Larson et al. in 2010 (Eq. (6)) to calculate Hs, Tp and direction at the closest grid point to the coast. This method has been validated by the properties of deep-water waves (Larson et al., 2010).

$$h_b = \frac{\lambda C^2}{g} \tag{6}$$

$$\alpha_b = \text{asin}\left(sin\left(\alpha_0\sqrt{\lambda}\right)\right) \tag{7}$$

with $\lambda = \Delta\sqrt{\lambda_a}$; considering

$$\Delta = 1 + 0.1649\xi + 0.5948\xi^2 - 1.6787\xi^3 + 2.8573\xi^4 \tag{8}$$

Table 3
Characteristics of satellite images used for monthly and interannual variability.

Satellites (sensor)	GEE collection	Date of acquisition (yyyy/mm)	Number of images
Landsat 5 (TM)	LANDSAT/LT05/ C01/T1_TOA	1986/01-1999/01	15
Landsat 7 (ETM)	LANDSAT/LE07/ C01/T1_RT_TOA	1999/09-2020/04	182
Landsat 8 (OLI)	LANDSAT/LC08/ C01/T1_RT_TOA	2013/04-2020/04	96
Sentinel 2A/2B (MSI)	COPERNICUS/S2	2015/09-2020/05	132

Table 4
Estimated errors calculated during data processing.

Measurement errors	Uncertainty (m) 1986–2020			
	Landsat 5	Landsat 7	Landsat 8	Sentinel 2
Georeferencing error (Eg)	5	2.5	2.5	1
Digitizing error (Ed)	±1.5	1.05	1.05	0.7
Tide error (Et)	/	5.24	4.28	2.04
Pixel size error (Ep)	30	15	15	10
Total shoreline position error (ET)				18.16
Annualize Error (EA)				0.55

$$\xi = \lambda_a sin\theta_0^2; \quad \lambda_a = [\cos(\alpha_0/\theta)]^{2/5}; \quad \theta = \left(\frac{C}{\sqrt{gh}}\right)^4 \left(C/C_g\right)\lambda^2 \tag{9}$$

hb wave height at wave break; T period (does not change as it propagates from the open sea to the coast); $\gamma = h_b/H$ wave breaking threshold following Battjes and Janssen (1978) H depth at the point of wave breaking, and finally $C_g = C/2$ the group velocity of waves propagating towards the coast and θ_0 and θ direction of waves in deep water and at the point of wave breaking respectively.

We averaged each series of data (coastline and Hs) on a monthly basis for each segment. Subsequently, a mean value was calculated and subtracted from each value in the data series (HsA). Seasonal signal were removed, using a least square fit to the sine functions, before calculating trends. The trend calculation was based on a simple linear regression fit.

$$-f(x) = a_n * \sin(b_n * x + c_n) \quad n \in \mathrm{N} \tag{10}$$

With a amplitude; b angular speed and c the phase shift.

3. Results

3.1. Coastal changes from 1986 to 2020

DSAS analyses indicate that 30.55% of Cameroon's shoreline are eroding, 27.70% are accreting and 41.75% are stable. Fig. 2c illustrates the longshore variation of the coastline during the period 1986 to 2020 following a period marked by deep and permanent changes in the estuaries (C1 and C3) of the Rio del Rey and Wouri estuaries respectively. Some areas were found to be stable (C2, Limbe), and some areas with small-scale shoreline changes were identified. e.g. C5 (Kribi Coast) with erosion and deposition rates ranging between −2.7 and 2.1 m/year, and only a minor displacement of the shoreline of 10 m between 2010 and 2013 observed on the northern coast of Kribi (Fig. 2a). The maximum observed erosion occurred at Rio del Rey and Cap Cameroon (C3) with significant shoreline retreats of up to −15 to −8 m /year (Figs. 2a and 2c).

Table 5 shows small changes (between 0.43 and 0.65 m/year) in the Kribi (C5) and Limbé (C2) segment. Significant and very localized changes are observed with an erosion of −11 to −6 m/year respectively in C1 and C3. Section (see above on section, part, segment.…) C4 is accumulating while parts C1 and C3 are heavily eroding. An illustration is made by the diagram in Fig. 2a, which shows permanent erosion well before the year 1988.

3.2. Validation of coastline positions derived from satellite imagery with in-situ measurements

To ground-truth satellite-based data, satellite-derived results were compared with field data at C2 and C5 (Fig. 3). Data from other sections are not available. The comparison indicates that the satellites are able to well identify the main horizontal coastline changes (r = 0.84 for C5 and 0.79 for C2).

3.3. Seasonal coastline variability and wave regime

The results of the seasonal analysis of shoreline changes and waves are shown in Fig. 4. It is noted that the seasonal variation of the shoreline presents two different phases, an accretion phase in dry season (November to February/March) and an erosion phase in rainy season (April to October). During this later phase, the maximum erosion is reached in June except in C5 where the maximum is reached in August (−2 ± 0.32 m). The wave regime (anomaly HsA) is characterized by summer waves with a significant monthly mean height between 1.2 m and 1.7 m respectively in segments C1 and C5. Summer HsA are highest near C5 and lowest at C1 to C2 (northern part). It is during periods of high turbulence that significant erosional disturbance of the shoreline is observed. Note that a delay is generally observed between high HsA values and shoreline movement. During the winter (September to February), Hs values are almost below the annual average in all segment (Fig. 4).

3.4. Interannual coastline and wave height variability

Interannual analyses (Fig. 5) show significant fluctuations of the coastline from one year to another and from one site to another. The interannual evolution of the coastline shows three main periods of significant change from one segment to another. In segment C1, there was a marked retreat of the coastline during the first period (1986–1994), of the order of −3 ± 1.4 m. HsA peaked in 1990 and subsequently declined with a trend of −0.0047 m/year. Significant accretion shifts began to occur in the second period (1994 to 2005). In the final period (2006–2020) the shoreline oscillated between erosion and accretion. In C2, the first two periods are marked by a regressive trend of the order of −4 ± 0.2 m, followed by a period of accretion during the third period (2006–2020). Segment C3 is marked by a pronounced shoreline retreat of −9.4 ± 0.7 m over the 1986–1996 period. As in C1, the second period shows an accretion trend of 0.8 ± 0.0021 m/year, followed by a period of erosion (1994–2005). Segment C4 is relatively stable with time, marked by some punctual periods of

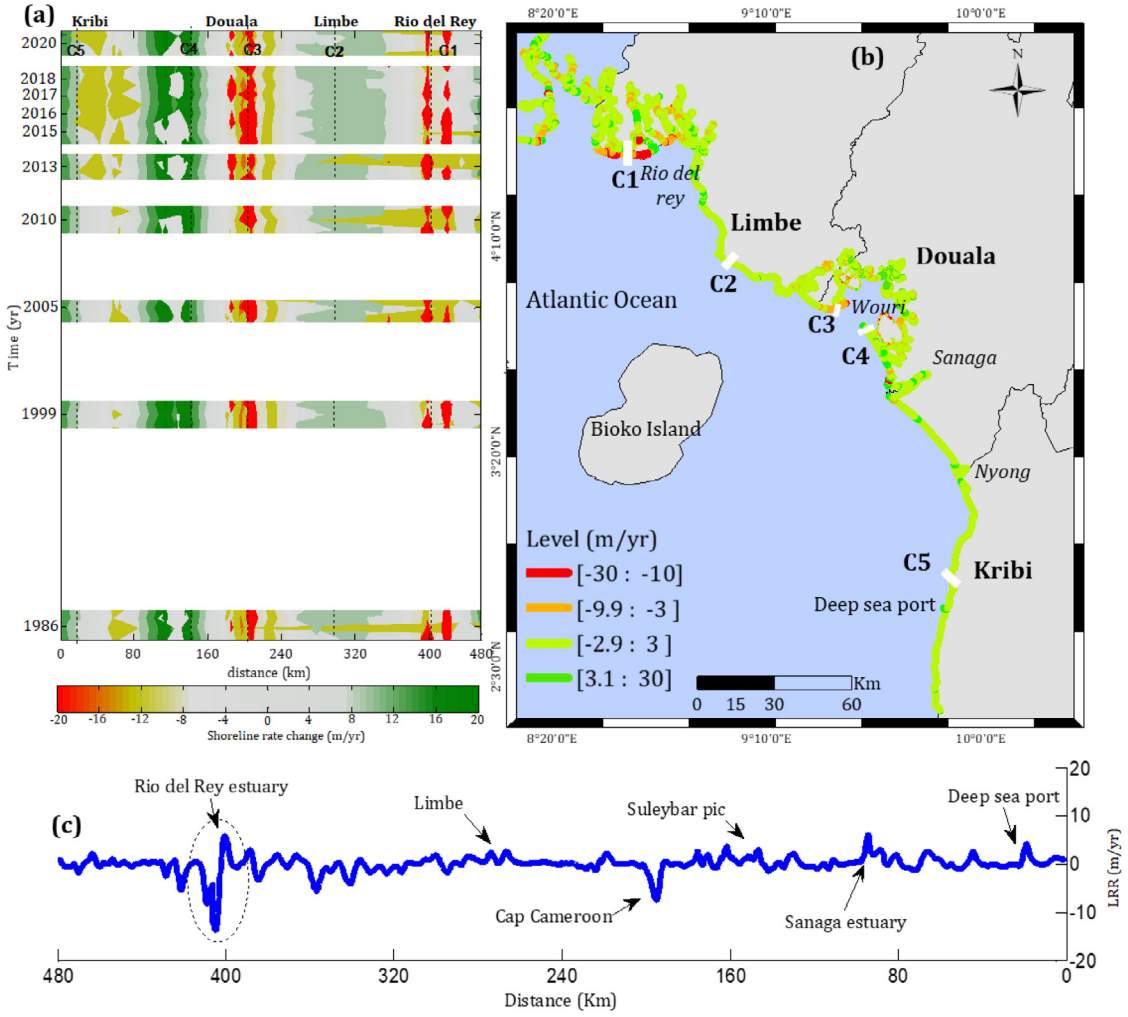

Fig. 2. Map of spatio-temporal changes showing erosion/accretion evolution. (a) Hovmoller diagram rate of change; (b) Overall coastline placement rate with sub-areas of interest identified (transepts: white dash C1 to C5); (c) Net rate of shoreline change between 1986–2020 showing a linear velocity trend along the coastline.

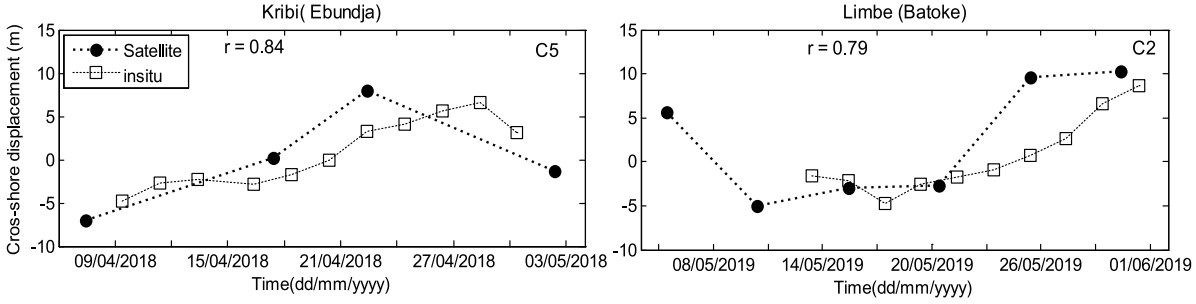

Fig. 3. Difference in across-shore displacement between in situ and satellite measurements (Kribi C5 and Limbé C2).

Table 5
Area change and overall observed displacement rate by area of interest.

	Kribi (C5)	Suleybar pic (C4)	Cap Cameroon (C3)	Limbe (C2)	Rio del rey (C1)
Surface (km^2)	11.5	8.21	6.4	8.24	25.87
Displacement rate (m/yr)	0.65 ± 0.04	5.87 ± 0.78	−6.05 ± 1.43	0.43 ± 0.05	−11.601 ± 4.02
Observation (1986–2020)	Stable	strong accretion	erosion	weak accretion	strong erosion

erosion and accretion. In C5 a maximum interannual progradation of the coastline of 10 ± 1.45 m was reached in 1989 followed by a long period of average stability of 0.76 ± 1.3 m (1995–2005). A continuous regression of the order of −5 ± 0.23 m was observed during the period 2008 to 2015. Linear regression analysis for shoreline changes from 1986 to 2020 showed a general erosion trend of ∼−6.2 m/year during the first period (1986–1994) and accretion trends during the second period (1995–2005) of 2.4

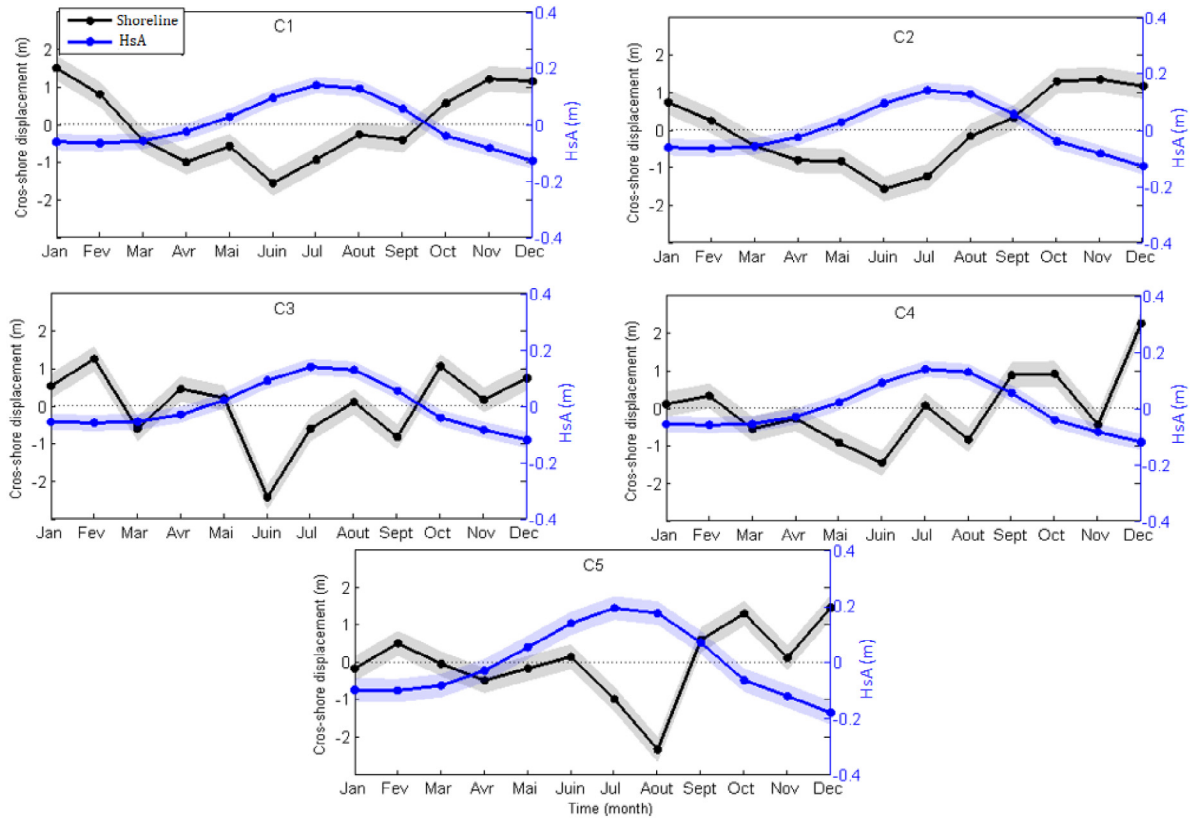

Fig. 4. Monthly variation in coastline and waves by segment (C1 to C5). Mean values and uncertainties (± standard deviation) are shown. The monthly coastlines are derived from the processing of the 425 GEE archive images via the CoastSat Toolbox. The blue curve represents the monthly variation in wave height anomaly, while the black curve represents the monthly coastline changes during the period 1986–2020. (For interpretation of the references to colour in this figure legend, the reader is referred to the web version of this article.)

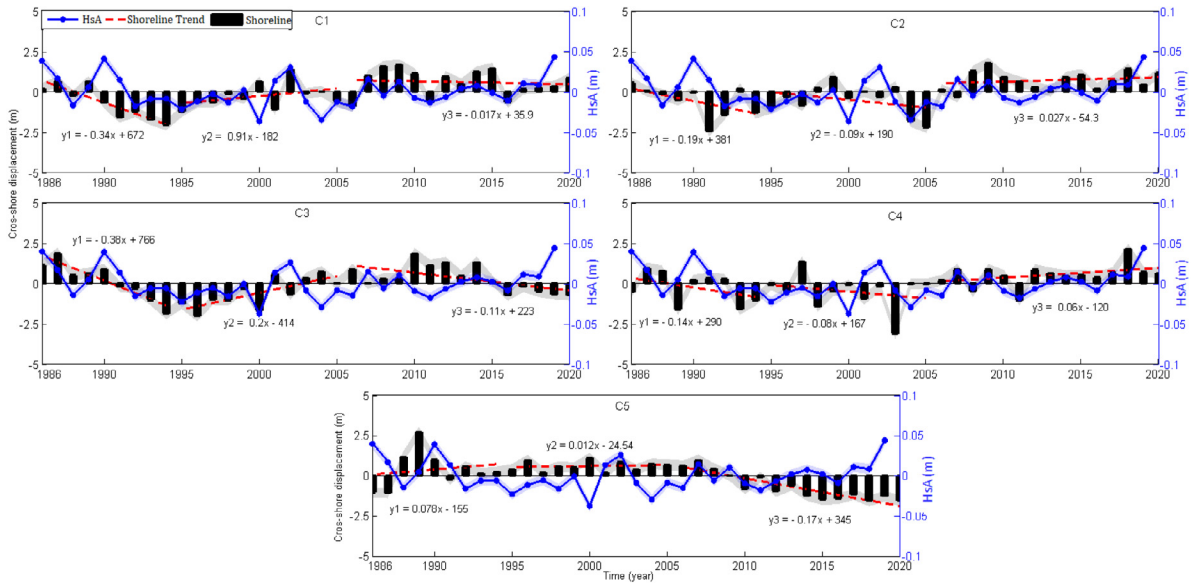

Fig. 5. Interannual coastline and wave variability anomaly HsA by segment (C1 to C5). The coastline trend is represented by the red line; uncertainties are also associated with the curves (± standard deviation). These results are derived from the processing of the 425 GEE archive images via the CoastSat Toolbox. (For interpretation of the references to colour in this figure legend, the reader is referred to the web version of this article.)

m/year (Fig. 5). The final period (2006–2020) is dominated by low-scale erosion of the order of −1.3 ± 0.75 m.

The interannual variation of waves in each segment (C1 to C5) shows a weak and constant wave climate distribution (Tp = 7 to 12 s in N–NW direction), the annual mean of Hs varies from 0.7 to 1.7 m with maximum of 1.7 ± 0.12 mm in C5. The interannual wave variability anomaly HsA Fig. 5 (C1–C5), shows an overall decrease in height during the first period of 1986–1994 with an annual downward trend at all segments (−0.0056 to −0.0041 m/year). Despite a significant fluctuation observed from 1999 to 2001, the second period (1995 to 2005) is marked by a relative stability in wave heights (trend between 0.0002

Table 6
Correlation coefficients between coastline and wave trend at interannual scale.

Correlation ΔX & Hs	Kribi (C5)	Suleybar pic (C4)	Cap Cameroon (C3)	Limbe (C2)	Rio del rey (C1)
1986–1994	−0.17	**0.27**	**0.27**	**0.26**	**0.25**
1995–2005	0.1.5	−0.15	0.005	0.0.08	0.0025
2005–2020	−0.17	**0.25**	**−0.42**	0.12	−0.10

and 0.0006 m/year) on the whole coast. The third period (2006–2019) is characterized by annual upward trends of Hs (0.0017 to 0.003 m/year) with an amplitude that increases towards the south (i.e. from segment C1 to C5). Distinct peaks characterized by values of Hs above the annual average as shown in Fig. 5 (C1 to C5), were observed in 1986, 1990, 2002 and 2019.

Interannual coastal changes were correlated to wave climates and the results are shown on Table 6. The variability of wave climate is less correlated and suggests that wave action could be significant with the coastline dynamics during the first period (1986–1994), with a correlation coefficient $r^2 = 0.25$ in segments C1 to C4. While between 2005 and 2020, the wave regime could be responsible for the erosion observed at C3 ($r = -0.42$). Overall, these results indicate that waves do not fully explain the high variability along the coastline. However, the involvement of waves makes it possible to understand more than 40% of the coastline dynamics in certain segments.

3.5. Spatial and temporal patterns in shoreline variability

An analysis of localized variability shows a dis-proportionality from one area to another. Taking into account the local characteristics (nature of the coastal substrate) allows to highlight the influence of waves on the morphological configuration of the coasts (Fig. 6a). However, the trend is reversed when we move to large time scales from 2012 onwards (Fig. 6b). This observation is even more evident on 10-year time scales (Fig. 6b). Fig. 6b shows two periods with erosive dominance regardless of the time scale of observation (C1 and C3). On the other hand, the Kribi zone experienced a first period (1992–2000) during which its northern part was slightly eroded, followed by a second period (2013–2019) with a migration and enlargement of the eroded zone and a concentration of an accumulation zone further south (Fig. 6a and Fig. 2 a and b).

Zone C2, for its part, is characterized by relative overall stability, although accompanied by regressive instability during 1991 and 2004, a period during which maximum variations in wave height were observed.

Part C3 (Cape Cameroon) experienced regressive coastline migration for nearly two decades (1986–2004). The variations observed in C3 during the 1986–2004 period were accompanied by strong wave activity (1.35 ± 0.4 m), creating a significant trend in cumulative erosion estimated at around −10 m/year. A different dynamic emerges from 2007, characterized by a permanent stability until the end of the study. Less significant and almost uniform variations are observed in C4, with a progressive formation of a sandy spit. The seasonal wave signal, although weak and permanent, is consistent with these slow changes (Fig. 4 — C4).

To examine causal factors for spatial and temporal variations in more detail, an analysis of the empirical orthogonal function (EOF) of the generated shoreline change and wave data was performed. The EOF analysis results show two modes (Fig. 6a) in each segment. Mode 1 accounts for 76.3% of the variability and mode 2 explains 23.7% of the variability. Based on a similar study carried out in the Bight of Benin in West Africa (Anthony et al., 2019), mode 1 may be related to small scales associated with relatively pronounced local erosion/accretion changes caused by natural shoreline dynamics. Mode 2 can be interpreted as representing a larger scale associated with the progressive decrease in accretion from south to north over the study period (Fig. 6b).

4. Discussion

The results of this study on shoreline changes at seasonal to decadal-scale along the Cameroonian coastline from 1986 to 2020 reveal a complex spatial configuration segmented along the coast and three temporal phases (1986 to 1994, 1995 to 2005, 2006 to 2020) were identified and characterized by significant fluctuation of the coastline.

The high rate of overall shoreline displacement observed at the estuary entrances (C1 and C3) is characterized by sandbars at the mouths that not only move over time but interact with the shoreline. However, one source of error in the position of these sandbars could be due to the time of image acquisition, which depends not only on the seasonal variability of river runoff, but also on oceanic forcing (Onguene, 2015). Although, Cameroonian rivers are characterized by high flows, (Rio del Rey (C1), Wouri, one of the largest in the sub-region (C3 and C4), and Sanaga (Fig. 2)), coastal currents in these estuaries have also been identified as responsible for the variability of sediment inputs that affect not only the dynamics of the coastline but also the seasonal sediment transport (Abessolo Ondoa et al., 2018).

The strong erosion trends during the first period (1986 to 1994) in segments C1 and C3 could be attributed to the cutting of mangroves amplified by an increase in sea level, and a resulting reduction in absorption of wave energy reaching the coast (Onguene et al., 2015). On the other hand, the work Almar et al. (2015) demonstrated that this can be attributed to two distinct and simultaneous processes: on the one hand, the decrease in southwest swells generated by mid-latitude storms, and on the other hand, the increasing contribution of secondary southeast swells (which will cause westward coastal transport, thus reducing the net eastward coastal transport) generated by positive trade anomalies. Nevertheless, further work is needed on these coastal processes to better understand the erosion phenomenon.

Segments C2 and C4 (Limbé and Pointe de Souleyba) are characterized by moderate to significant accretion rates of 2.4 m/year and 15.5 m/year, dominated by natural shoreline modification patterns, such as the Souleyba spit (C4). This backside would result from very complex dynamic of the convergence of the discharge of Wouri and Dibamba rivers associated with the littoral drift at the origin of the accretion observed in this segment (Abessolo Ondoa et al., 2018). The rate of change of shoreline displacement remains relatively stable in segment C2, as the lithological nature is characterized by the presence of cohesive sediments and rocky coasts as well as a coast dominated by the presence of mangroves and vegetation.

In the southern part C5, an abrupt change in dynamics is observed as of late 2013, likely due to the construction of a 1.5 km offshore oriented dike at the port of Kribi (30 km to the south of Kribi) in late 2013. The amount of sediment bypassing the dike may not sufficient to balance the high transport potential in this area (Fig. 2a, b). But also the presence several beach sand extraction quarries for construction with volume of more than 45,000 m3/year of extracted sediment on the Kribi coast (MINEPDED-RCM, 2017). These results corroborate with other studies that have shown that human activities would alter balance between sediment input and coastal erosion which leads to a progressive degradation of the coastal system (Rovira and Ibàñez, 2007; Batalla et al., 2004; Sanchez-Arcilla et al., 1998). The interannual wave variability obtained in the present study shows a gradual increase in HsA reaching the peak in 1990. The order of magnitude of the increasing trends in mean HsA (0.0017 to 0.003 m/year; Fig. 5) found in the present study, particularly from 2005 to 2020, are in line with the results of many studies carried out in the Gulf of Guinea sub-region (Dada et al., 2015; Anthony et al., 2019). Several ocean wave studies have reported an increase in Hs

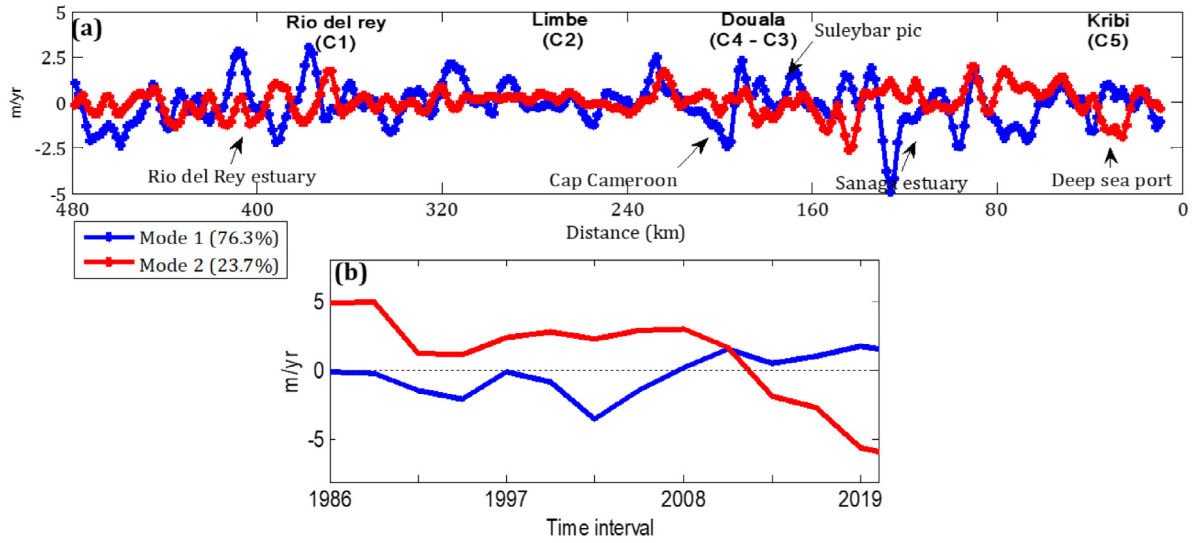

Fig. 6. Maps of contributions to shoreline change: (a) Spatial mode EOF (mode1: 76.3% of total variance) and EOF2 (mode2: 23.7% of total variance); (b) Temporal mode expressing the temporal behaviour of the rate of change.

in the North Atlantic Ocean in recent decades (e.g., Bertin et al., 2013; Le Cozannet et al., 2011; Dodet et al., 2010). Bertin et al. (2013) observed an increase in Hs over the entire North Atlantic Ocean based on numerical analysis of retrospective winds (1900 to 2008), reaching 0.01 m/yr and gradually decreasing to less than 0.005 m/yr in the southern North Atlantic. We also note the lack of validation of the Era-Interim data in the bottom of Gulf of Guinea, but also the very simplistic approach of Larson's formulation on the propagation of wave height from the open ocean to the coast that may not be realistic from coast to coast. The results obtained by (Dada et al., 2016) in the coast of the Niger Delta (upper limit of Bonny Bay), are slightly larger but of the same order of magnitude as that obtained in our study. This could be explained by the fact that the work of (Dada et al., 2016) was calculated over a much longer period (last 110 years) with a maximum increase in HsA of 0.0054 m/year. The seasonal rhythm of the coastline indicates a period of erosion corresponding to the passage of the ITCZ over the equatorial zone characterized by heavy rainfall. During this period of heavy agitation (May to September), wave heights anomaly increase and the coast undergoes significant disturbance. Similar results from Almar et al. in 2015 demonstrated that the equatorial fluctuation of the Intertropical Convergence Zone (ITCZ) explains most of the variability in wave-induced transport but also the predominant influence of the Southern Annular Mode (SAM) on wave-induced transport. Climate change, sea level rise, marine submersion and degradation of coastal vegetation could also induce profound changes in the nearshore in the long term.

In this study, the results of the analysis of EOF variability patterns of spatial–temporal shoreline changes show two modes. Mode 1 (76.3%) show that the wave regime does not fully explain the changes observed on the Cameroonian coast. For the decrease in wave height from the southern to the northern part of our study area in which we find two important hotspot C1 (Rio del rey)and C3 (Wouri estuary), with high tidal range (Onguene et al., 2015) in this northern part than in the southern part of the coast, testifies to predominance of other factors. However, recent work by Abessolo Ondoa et al. (2018) showed that barotropic currents exiting the Wouri estuary were also responsible for the erosive process at Cape Cameroon (C3). Add to these currents, the variability of sediment from the upstream of the rivers to the mouth, which is controlled by the seasonal fluctuation of flows and sediment transport, which some authors have shown to be directly or indirectly related to the climatic variability of rainfall in the river basin of the area (Mahe et al., 2001; Bricquet et al., 1997a). Aguilar et al. (2009) showed that despite the increase in heavy rainfall over the last half century, Central Africa has shown a significant decrease. Mahe et al. (2001) also showed that a break period with a deficit of rainfall was observed in the Gulf of Guinea area from 1951 to 1989. We can say that, this downward trend observed in the long-term rainfall series of the equatorial units has, that led to a significant decrease in the interannual mean flows of equatorial rivers (Olivry et al., 1993; Mahé and Olivry, 1999) would also be the cause of the sediment imbalance in Bonny Bay. This could be linked to a change in the monthly distribution of rainfall, as well as to the effect of certain drought years, as already described by Mahé et al. (1990) for the Ogooue River in Gabon.

The more localized work by Yontchang (2012) presents a net decrease in average rainfall of about −13.9% and −11.7% respectively in Douala and Bertoua with a statistical test of significance (p-value = 0.0003; 0.003). It also corroborates the observations of Lienou (2007) who notes that deficits in the transport of suspended solids by rivers were recorded during periods of reduced rainfall in some watersheds in Cameroon. All of these authors strongly argue that climate variability in this part of Central Africa has varied over the 20th century with marked internal variations, such as river flow, sediment transport and drought, with devastating environmental consequences in the sub-region.

The second mode (23.7%) could represent larger scale changes between mainly tidal currents which could be considered as having more influence than waves in the northern part where the erosion hotspots are located (C1, C3) near the estuaries mouths. At shorter seasonal scales, tidal currents (cross-shore transport) seem to be one of the dominant factors in the evolution of the coastline and are all the stronger during ebb tides but also when they encounter a constricted passage area such as estuaries (Dada et al., 2016). However, crossshore erosion/accretion processes progressively disappear with increasing temporal scale (Pinto et al., 2009). A similar phenomenon occurs in the Calabar estuary on the adjacent Nigerian coast, where the tidal range is ∼3 m and the ebb current is dominant. In addition to the involvement of tidal currents, longshore sediment transport processes are one of the main factors controlling the evolution of the Cameroonian coastline. These results further corroborate with the work of several authors (Awosika et al., 2013; Sexton and Murday, 1994; Ibe

and Antia, 1983; Allen, 1965; NEDECO, 1961; Dada et al., 2016). These longshore drift currents induce an important sediment transport parallel to the coast whose construction of protective structures such as the dike of the port of Kribi located on the southern part (C5) could impact the balance of sediment transit by trapping sediments upstream of the structure, and causes erosion downstream following the direction of the longshore current in the longer term.

5. Conclusion

The evolution of the coastline based on a 34-year time series (1986 to 2020) of satellite image data (Earth Explorer and GEE) and the Era-interim re-analysed wave data improved the understanding of coastline variability and local and regional wave climate in the study area. The shoreline change analysis undertaken here reveals a permanent and localized erosive trend on two segments (C1 and C3) over the 402 km along the Cameroonian coast. Nevertheless, a seasonal signal on coastline variability is evident, corroborated by the strong interannual variability in local and regional wave climate. The EOF analysis has highlighted two modes of variability representing respectively the local spatiotemporal scale influence mode 1, but also a larger scale influence mode 2. While this study suggest that shoreline changes are not only related to local and regional wave climate variability, it is important to note that shoreline stability is also strongly dependent on a constant supply of sediments, and other processes such as: variability of river discharge in sediment transport that could be directly influenced by the rainfall regime; tidal currents, longshore drift currents, and anthropogenic activities, may act in combination with climate changes to influence shoreline changes along the Cameroonian coast.

CRediT authorship contribution statement

Njutapvoui F. Nourdi: Conceived and designed the study, Formal analysis, Writing - original draft, Data processing. **Onguene Raphael:** Conceived and designed the study, Formal analysis, Writing - original draft. **Abessolo O. Grégoire:** Data processing, Formal analysis, Writing - original draft. **Rudant Jean Paul:** Conceived and designed the study, Formal analysis, Writing - original draft, Data processing. **Bogning Sakaros:** Data processing, Formal analysis, Writing - original draft. **Stieglitz Thomas:** Formal analysis, Writing - original draft. **Tomedi E. Minette:** Formal analysis, Writing - original draft.

Declaration of competing interest

The authors declare that they have no known competing financial interests or personal relationships that could have appeared to influence the work reported in this paper.

Acknowledgements

This project was funded by the *service de coopération et d'Action Culturelle* (SCAC) of the French Embassy in Cameroon within the framework of a research mobility grant awarded to Njutapvoui Nourdi, as part of a co-supervision agreement between the University of Douala (UDo_EDSFA) and the University Paris Est Marne la Vallée. We used data provided though the ECMWF ERA Interim dataset (www.ECMWF.Int/research/Era), Landsat images downloaded from https://earthexplorer.usgs.gov/, Google Earth Engine (GEE) and Sentinel images from the ESA Copernicus program.

References

Abessolo Ondoa, G., Onguéné, R., Tomedi Eyango, M., Duhaut, T., Mama, C., Angnuureng, B.D., Almar, R., 2018. Assessment of the evolution of Cameroon coastline: An overview from 1986 to 2015. In: Tropical Coastal and Estuarine Dynamics. J. Coast. Res. (ISSN: 0749-0208) (81), 122–129, Special Issue, Coconut Creek (Florida).

Aguilar, E., et al., 2009. Changes in temperature and precipitation extremes in western central Africa, Guinea Conakry, and Zimbabwe, 1955–2006. J. Geophys. Res. 114, D02115. http://dx.doi.org/10.1029/2008JD011010.

Ajonina, G.N., 2010. Rapport final de réalisation du mandat. In: Consultation Project GEF PPG. p. 36.

Allen, J.R.L., 1965. Late Quaternary Niger Delta and adjacent areas: sedimentary environment sand lithofacies. Bull. Am. Assoc. Pet. Geol. 48, 547–600.

Almar, R., Honkonnou, N., Anthony, E.J., Castelle, B., Senechal, N., Laibi, R., Mensah-Senoo, T., Degbe, G., Quenum, M., Dorel, M., Chuchla, R., Lefebvre, J.P., Du Penhoat, Y., Laryea, W.S., Zodehougan, G., Sohou, Z., Addo, K.A., Ibaceta, R., Kestenare, E., 2014. The Grand Popo beach 2013 experiment, Benin, West Africa: From short timescale processes to their integrated impact over long-term coastal evolution. In: Green, A.N., Cooper, J.A.G. (Eds.), Proceedings 13th International Coastal Symposium (Durban, South Africa). J. Coast. Res. (70), 651–656, Special Issue.

Almar, R., Kestenare, E., Reyns, J., Jouanno, J., Anthony, E.J., Laibi, R., Hemer, M., Du Penhoat, Y., Ranasinghe, R., 2015. Response of the Bight of Benin (Gulf of Guinea, West Africa) coastline to anthropogenic and natural forcing, Part1: Wave climate variability and impacts on the longshore sediment transport. Cont. Shelf Res. 110, 48–59.

Anthony, E.J., 2017. Beach erosion. In: Finkl, C., Makowski, C. (Eds.), Encyclopedia of Coastal Science. In: Encyclopedia of Earth Sciences Series, Springer, Cham.

Anthony, E.J., Almar, R., Besset, M., Reyns, J., Laibi, R., Ranasinghe, R., Abessolo Ondoa, G., Vacchi, M., 2019. Response of the Bight of Benin (Gulf of Guinea, West Africa) coastline to anthropogenic and natural forcing, Part 2: Sources and patterns of sediment supply, sediment cells, and recent shoreline change. Cont. Shelf Res. 173, 93–103. http://dx.doi.org/10.1016/j.csr.2018.12.006.

Anthony, E.J., Blivi, A.B., 1999. Morphosedimentary evolution of a delta-sourced, drift-aligned sand barrier-lagoon complex, western Bight of Benin. Mar. Geol. 158, 161–176. http://dx.doi.org/10.1016/S0025-3227(98)00170-4.

Awosika, L.F., Folorunsho, R., Imovbore, V., 2013. Morphodynamics and features of littoral cell circulation observed from sequential aerial photographs and Davies drifter along a section of the strand coast east of the Niger Delta. Nigeria. J. Ocean. Mar. Sci. 4 (1), 12–18.

Batalla, R.J., Gomez, C.M., Kondolf, G.M., 2004. Reservoir-induced hydrological changes in the Ebro River basin (NE Spain). J. Hydrol. 290, 117–136.

Battjes, J.A., Janssen, J.P.F.M., 1978. Energy loss and setup due to breaking of random waves. In: Proceedings of the ASCE International Conference on Coastal Engineering, Hamburg, Germany, 1978, pp. 569–587.

Bertin, X., Prouteau, E., Letetrel, C., 2013. A significant increase inwave height in the North Atlantic Ocean over the 20th century. Glob. Planet. Chang. 106 (77).

Boateng, I., 2009. Development of integrated shoreline management planning: A case study of keta, Ghana. In: TS 4E—Coastal Zone Management. FIG Working Week 2009. Surveyors Key Role in Accelerated Development Eilat, Israel. pp. 3–8.

Boateng, I., 2012. An application of GIS and coastal geomorphology for large scale assessment of coastal erosion and management: a case study of ghana. J. Coast. Conserv. 16, 383–397. http://dx.doi.org/10.1007/s11852-012-0209-0.

Bosom, E., Jiménez, J.A., 2011. Probabilistic coastal vulnerability assessment to storms at regional scale - application to Catalan beaches (NW Mediterranean). Nat. Hazards Earth Syst. Sci. 11, 475–484.

Bricquet, J.P., Bamba, F., Mahé, G., Touré, M., Olivry, J.-C., 1997a. Evolution récente des ressources en eau de l'Afrique Atlantique. Revue des Sciences de l'eau 3, 321–337.

Caires, S., Swail, V.R., Wang, X.L., 2006. Projection and analysis of extreme wave climate. J. Clim. 19, 5581–5605.

Dada, O.A., Li, G., Qiao, L., Ma, Y., Ding, D., Xu, J., Yang, J., 2016. Response of waves and coastline evolution to climate variability off the Niger Delta coast during the past 110years. J. Mar. Syst. 160, 64–80. http://dx.doi.org/10.1016/j.jmarsys.2016.04.005.

Dada, O.A., Qiao, L.L., Ding, D., Li, G.X., Ma, Y.Y., Wang, L.M., 2015. Evolutionary trends of the Niger Delta Shoreline during the last 100 years: responses to rainfall and river discharge. Mar. Geol. 367, 202–211. http://dx.doi.org/10.1016/j.margeo.2015.06.007.

Dee, D.P., Uppala, S.M., Simmons, A.J., Berrisford, P., Poli, P., Kobayashi, S., Andrae, U., Balmaseda, M.A., Balsamo, G., Bauer, P., Bechtold, P., Beljaars, A., Van De Berg, L., Bidlot, J.R., Bormann, N., Delsol, C., Dragani, R., Fuentes, M., Geer, A.J., Haimberger, L., Healy, S., Hersbach, H., Hólm, E.V., Isaksen, L., Kållberg, P.W., Köhler, M., Matricardi, M., McNally, A., Monge-Sanz, B.M., Morcrette, J.J., Peubey, C., De Rosnay, P., Tavolato, C., Thépaut, J.N., Vitart, F., 2011. The ERA-interim reanalysis: Configuration and performance of the data assimilation system. Q. J. R. Meteorol. Soc. 137 (656), 553–597.

Dodet, G., Bertin, X., Taborda, R., 2010. Wave climate variability in the North East Atlantic over the last 6 decades. Ocean Model. 31, 120–131.
Fernand, Verger, Ghirardi, Raymond, et al., 2002. L'Espace Nouveau Territoire : Atlas Des Satellites Et Des Politiques Spatiales, Paris, Belin. p. 383, ISBN 978-2-701-13194-8 et 2-701-13194-4 OCLC 51653010.
Fotsi, Pouvreau, Brenon, Onguene, Etame, 2019. Temporal (1948–2012) and dynamic evolution of the wouri estuary coastline within the gulf of guinea. J. Mar. Sci. Eng. 7 (10), 343. http://dx.doi.org/10.3390/jmse7100343.
Giardino, A., Schrijvershofa, R., Nederhoffa, C.M., de Vroega, H., Brièrea, C., Tonnona, P.-K., Cairesa, S., Walstraa, D.J., Sosac, J., van Versevelda, W., Schellekensa, J., Sloffa, C.J., 2018. A quantitative assessment of human interventions and climate change on the West African sediment budget. Ocean Coast. Manag. 156, 249–265.
Giresse, P., Megope, F.J., Ngueutchoua, G., Aloisi, J.C., 1996. Carte Sédimentologique Du Plateau Continental Du Cameroun. Paris, France: ORSTOM, Collection Notice Explicative N° 111. p. 12.
Hapke, C.J., Himmelstoss, E.A., Kratzmann, M., List, J.H., Thieler, E.R., 2010. National Assessment of Shoreline Change: Historical Shoreline Change Along the New England and Mid-Atlantic Coasts: US Geological Survey Open-File Report 2010-1118. p. 57.
Ibe, A.C., Antia, E.E., 1983. Preliminary assessment of the impact of erosion along the Nigerian shoreline. In: NIOMR Tech. Pap. No 13. p. 18.
Kuenzer, C., van Beijma, S., Gessner, U., Dech, S., 2014. Land surface dynamics and environmental challenges of the Niger Delta, Africa: remote sensing-based analyses spanning three decades (1986–2013). Appl. Geogr. 53, 354–368.
Laibi, R.A., Anthony, E.J., Almar, N., Castelle, B., Sénéchal Kestenare, E., 2014. Longshore drift cell development on the human-impacted Bight of Benin sand barrier coast. West Africa. J. Coast. Res. 78–83, (Special 70).
Larson, M., Hoan, L., Hanson, H., 2010. Direct formula to compute wave height and angle at incipient breaking. J. Waterway Port. Coast. Ocean Eng. 136, 119–122.
Le Cozannet, G., Lecacheux, S., Delvallee, E., Desramaut, N., Oliveros, C., Pedreros, R., 2011. Teleconnection pattern influence on sea-wave climate in the Bay of Biscay. J. Clim. 24 (3), 641–652.
Lienou, Gaston, 2007. Impacts de la variabilité climatique sur les ressources en eau et les transports de matières en suspension de quelques bassins versants représentatifs au Cameroun. In: Thèse de Doctorat Ph/D En Sciences de L'Eau. p. 253.
Luijendijk, A., Hagenaars, G., Ranasinghe, R., Baart, F., Donchyts, G., Aarninkhof, S., 2018. The state of the world's beaches. Sci. Rep. 1–11. http://dx.doi.org/10.1038/s41%20598-018-24630-6.
Mahé, G., Lerique, J., Olivry, J.-C., 1990. Le fleuve Ogooué au Gabon. Reconstitution des débits manquants et mise en évidence de variations climatiques à l'équateur. Hydrol. Cont. 5 (2), 105–124.
Mahe, G., L'hote, Y., Olivry, J.C., Wotling, G., 2001. Trends and discontinuities in regional rainfall of West and Central Africa: 1951-1989. Hydrol. Sci. J. 46 (2), 211–226. http://dx.doi.org/10.1080/02626660109492817.
Mahé, G., Olivry, J.C., 1999. Assessment of freshwater yields to the ocean along the intertropical coast of Africa (1951-1989). C. R. Acad Sci. Paris 3 (28), 621–626.
MINEPDED-RCM, 2017. Etat des lieux des mangroves du cameroun. In: Ministère de L'Environnement, de la Protection de la Nature Et Du Développement Durable En Collaboration Avec Le Réseau Camerounais Des Mangroves. P. 10-11.
Moore, L.J., Griggs, G.B., 2002. Long-term cliff retreat and erosion hotspots along the central shores of the Monterey Bay National Marine Sanctuary. Mar. Geol. 181 (1-3), 265–283.
Morin, S., et Kuété, M., 1988. Le littoral Camerounais: problèmes morphologiques. In: Travaux Du Laboratoire de Géographie Physique Appliquée. No 11. pp. 5–52.
Ndour, A., Laïbi, R., Sadio, M., Degbé, C.G.E., Diaw, A.T., Oyédé, L.M., Anthony, E.J., Dussouillez, P., Sambou, H., Dièye, E.H.B., 2018. Management strategies for coastal erosion problems in West Africa: Analysis, issues, and constraints drawn from examples from Senegal and Benin. Ocean Coast. Manag. 156, 92–106. http://dx.doi.org/10.1016/j.ocecoaman.2017.09.001.
NEDECO, 1961. The waters of the Niger Delta. Hague 143.
Olivry, J.C., 1986. Fleuve et rivière du Cameroun, MESRES-ORSTOM. In: Collection Monographie Hydrologique ORSTOM N 9 Paris.
Olivry, J.-C., Bricquet, J.P., Mahé, G., 1993. Vers un appauvrissement durable des ressources en eau de l'Afrique humide? In: Stuart, J.G. (Ed.) Hydrology of Warm Humid Regions. Proceedings of a joint IAMAS-IAHS symposium held at Yokohama, pp. 67-78. AISH pub. 216.
ONEQUIP, 2009. Contrat n 01090031 relatif à l'élaboration d'un programme de suivi de la vitalité des mangroves camerounaises. In: Projet CAPECE-CPSP/SNH. Rapport Final. p. 146.
Onguene, R., 2015. Modélisation Multi-Echelles de la Circulation Océanique En Afrique Centrale, de la Plaine Abyssale à L'Estuaire Du Cameroun. (Ph.D. dissertation). University of Toulouse III Paul Sabatier, Toulouse, France, p. 216.
Onguene, R., et al., 2015. Overview of tide characteristics in Cameroon coastal areas using recent observations. Open J. Mar. Sci. 5, 81–98. http://dx.doi.org/10.4236/ojms.2015.51008.
Pilkey, O.H., Cooper, J.A.G., 2014. Are natural beaches facing extinction? J. Coast. Res. 70, 78–83.
Pinto, C.A., Taborda, R., Andrade, C., Teixeira, S.B., 2009. Seasonal and mesoscale variations at an embayed beach (armação de Pera, Portugal). In: SI56 (Proceedings of the 10th International Coastal Symposium), 118–122. Lisbon, Portugal. J. Coast. Res. ISSN: 0749–0258.
Ranasinghe, R., 2016. Assessing climate change impacts on open sandy coasts: A review. Earth-Sci. Rev. 160, 320–332. http://dx.doi.org/10.1016/j.earscirev.2016.07.011.
Richards, J., Nicholls, R.J., 2009. Impacts of climate change in coastal systems in europe. In: PESETA Coastal Systems Study. JRC Scientific and Technical Reports, JRC 55390, EUR 24130 EN, European Commission, Joint Research Center, Luxembourg.
Robin, M., 2002. Télédétection et modélisation du trait de côte et de sa cinématique. In: Baron-Yelles, N., Goeldner-Gionella, L., Velut, S. (Eds.), Le Littoral, Regards, Pratiques Et Savoirs. Etudes Offertes à Fernand VERGER. Edition Rue D'Ulm / Presses Universitaires de L'Ecole Normale Supérieure, Paris, pp. 95–115.
Rovira, A., Ibàñez, C., 2007. Sediment management options for the lower Ebro River and its Delta. J. Soils Sed. 7 (5), 285–295.
Sanchez-Arcilla, A., Jimenez, J.A., Valdemoro, H.I., 1998. The Ebro Delta: morphodynamics and vulnerability. J. Coast. Res. 14 (3), 754–772.
Sexton, W.J., Murday, M., 1994. The morphology and sediment character of the coastline of Nigeria-the Niger Delta. J. Coast. Res. 10 (4), 959–977.
Stafford, D.B., Langfelder, J., 1971. Air photo survey of coastal erosion. Photogramm. Eng. 37, 565–575.
Sterl, A., Caires, S., 2005. Climatology, variability and extrema of ocean waves-the web-based KNMI/ERA-40 wave atlas. Int. J. Clim. 25, 963–977.
Tano, R.A., Aman, A., Kouadio, K.Y., Toualy, E., Ali, K.E., Assamoi, P., 2016. Assessment of the ivorian coastal vulnerability. J. Coast. Res. 32 (6), 1495–1503.
Thieler, E.R., Himmelstoss, E.A., Zichichi, J.L., Ergul, A., 2009. The Digital Shoreline Analysis System (DSAS) Version 4.0an ArcGIS Extension for Calculating Shoreline Change. Available at: http://woodshole.er.usgs.gov/project-pages/DSAS/version4/index.html.
Vos, K., Harley, M.D., Splinter, K.D., Simmons, J.A., Turner, I.L., 2019a. Subannual to multi-decadal shoreline variability from publicly available satellite imagery. Coast. Eng. 150, 160–174. http://dx.doi.org/10.1016/j.coastaleng.2019.04.004.
Vos, K., Splinter, K.D., Harley, M.D., Simmons, J.A., Turner, I.L., 2019b. Coastsat: A Google Earth Engine-enabled Python toolkit to extract shorelines from publicly available satellite imagery. Environ. Model. Softw. 104528. http://dx.doi.org/10.1016/j.envsoft.2019.104528.
Van der Walt, S., Scheonberger, J.L., Nunez-Iglesias, J., Boulogne, F., Warner, J.D., Yager, N., Gouillart, E., Yu, T., 2014. Scikit-image : image processing in Python. PeerJ 2, e453. http://dx.doi.org/10.7717/peerj.453.
Yontchang, G.D., 2012. Assessment and modelling of climate variability and change in Cameroon (central Africa). https://library.wmo.int/doc_num.php?explnum_id=2059 (see pages 15-17).